

See discussions, stats, and author profiles for this publication at: <https://www.researchgate.net/publication/5258545>

# Stimuli-Responsive Controlled Growth of Mono- and Bidimensional Particles from Basic Zirconium Sulfate Hydrosols

ARTICLE *in* THE JOURNAL OF PHYSICAL CHEMISTRY B · AUGUST 2008

Impact Factor: 3.3 · DOI: 10.1021/jp803039p · Source: PubMed

CITATIONS

9

READS

26

## 5 AUTHORS, INCLUDING:



**Marinalva Aparecida Alves-Rosa**

São Paulo State University

8 PUBLICATIONS 51 CITATIONS

[SEE PROFILE](#)



**Celso V Santilli**

São Paulo State University

237 PUBLICATIONS 3,020 CITATIONS

[SEE PROFILE](#)



**S.H. Pulcinelli**

São Paulo State University

185 PUBLICATIONS 2,446 CITATIONS

[SEE PROFILE](#)



**Valerie Briois**

French National Centre for Scientific Resea...

183 PUBLICATIONS 2,961 CITATIONS

[SEE PROFILE](#)

# Stimuli-Responsive Controlled Growth of Mono- and Bidimensional Particles from Basic Zirconium Sulfate Hydrosols

M. A. Alves Rosa,<sup>†</sup> C. S. S. Sanhueza,<sup>†</sup> C. V. Santilli,<sup>\*,†</sup> S. H. Pulcinelli,<sup>†</sup> and V. Briois<sup>‡</sup>

*Instituto de Química/UNESP, P.O. Box 355, CEP 14801-970 Araraquara, SP, Brazil, and Synchrotron SOLEIL, L'Orme des Merisiers, BP 48, 91192 Gif sur Yvette, cedex France*

*Received: April 8, 2008; Revised Manuscript Received: April 23, 2008*

A thermostimulated sol–gel transition in a system prepared by mixing a  $\text{ZrOCl}_2$  acidified solution to a hot  $\text{H}_2\text{SO}_4$  aqueous solution was studied by dynamic rheological measurements and quasi-elastic light scattering. The effect of temperature and of molar ratio  $R_S = [\text{Zr}]/[\text{SO}_4]$  on the gelation kinetics was analyzed using the mass fractal aggregate growth model. This study shows that the linear growth of aggregates occurs at the early period of transformation, while bidimensional growth occurs at the advanced stage. The bidimensional growth can be shifted toward monodimensional growth by decreasing the aggregation rate by controlling the temperature and/or molar ratio  $R_S$ . EXAFS and Raman results gave evidence that the linear chain growth is supported by covalent sulfate bonding between primary building blocks. At the advanced stage of aggregation, the assembly of linear chains through hydrogen bonding gave rise to the growth of bidimensional particles.

## 1. Introduction

The nanoscaled control of morphologies of nanobuilding blocks and their organization in complex hierarchic architecture or in periodic arrangement is a challenge of new technologies based on nanoscale machines and devices.<sup>1–3</sup> The emergent strategies to produce organized nanostructures combine dynamic and patterning properties of soft matter (liquid crystals, micelles, vesicles, emulsions, air–liquid foams, liquid–liquid foams, etc.) with the generation of a rigid network by sol–gel chemistry.<sup>3–6</sup> The success of this approach was illustrated in the preparation of nanostructure oxides, where the coassembling forces based on electrostatic or H-bonding interactions between surfactants and inorganic species give rise to the control of the periodic arrangement of the porous network of the final materials.<sup>1–6</sup> Despite the reversible nature of weak interactions involved in the self-assembly of organic molecules, their coassembling with a covalently bonded inorganic network transforms the organized soft matter into a hard stone-like structure, which hinders the reorganization of its supramolecular architecture in response to environmental conditions such as pH, salt concentration, or temperature changes. The stimuli-responsive feature of both the organic assembling and the surrounding reaction environment seems to be a requirement for the regulation of shape and patterning of inorganic materials with a complex form such as that found in the majority of natural biomaterials (bones, shells, teeth, coccolith, etc.).<sup>7,8</sup>

Classes of particularly important stimuli-responsive materials, which are able to simulate biological soft matter, are hydrogels formed by the physical or chemical cross-linkage of natural (collagen, hyaluronic acid, fibrin, alginate, agarose, and chitosan) or synthetic linear polymers.<sup>9</sup> A piece of hydrogel immersed in an aqueous environment can support the reversible change of volume by any stimulus that will change the polymer–environment interaction and hence the degree of swelling. Thus, a small

change in temperature, pH, and ionic or mechanical strength can cause an abrupt volume change. Among these materials, thermoreversible hydrogels have an interesting gelation behavior, which is reversibly responsive to temperature.<sup>9</sup> This phenomenon, which is characterized by an abrupt viscosity change, can be useful to induce transient instability and the subsequent temporal modulation of the patterning process. Although polymer hydrogels successfully were employed in the elaboration of different kinds of actuators including pulsate drug release, only a few groups have reported their use to prepare patterned inorganic materials.<sup>10</sup>

Besides the fact that the thermoreversible sol–gel transition is not commonly observed for inorganic systems, some years ago, we evidenced the possibility of preparing a kinetically stable sol and thermoreversible gel, by controlling the  $R_S = [\text{Zr}]/[\text{SO}_4]$  and  $R_{\text{Cl}} = [\text{Zr}]/[\text{Cl}]$  nominal molar ratios of the zirconyl chloride aqueous solution modified by sulfuric and hydrochloric acids.<sup>11–13</sup> Both kinetically stable and thermoreversible sols are formed by the same polynuclear species characterized by inner core oxo-hydroxo groups bridging together zirconium atoms surrounded on the surface by hydroxyl and sulfate ligands.<sup>12</sup> We proposed that these building blocks have a structure analogous to that determined for basic zirconium sulfate single crystals of  $\text{Zr}_{18}\text{O}_4(\text{OH})_{38.8}(\text{SO}_4)_{12.6} \cdot 33\text{H}_2\text{O}$ .<sup>14</sup> The thermoreversible sol–gel transition in this system is governed by the temperature-dependent ionic adsorption and ionic exchange capacities involving both  $\text{Cl}^-$  and  $\text{SO}_4^{2-}$  anions.<sup>13</sup> Recently, the possibility of combining this thermoreversible sol–gel system with a hexagonal swollen liquid crystal (SLC) to synthesize macroscopic fibers of zirconia presenting a hierarchic nanoscopic structure was presented.<sup>15</sup> However, the mechanism concerning the growth of these one-dimensional particles has not yet been elucidated.

The aim of the present work was to demonstrate that anisotropic zirconia-based particle growth in the complex environment discussed previously is under kinetic control, proceeding by the sequential modification of the surface and interface of the amorphous inorganic precursor. The dynamics of the thermo-induced aggregation and growth process of

\* Corresponding author. Tel.: +55-16 201 6645; fax: +55-16 222 7932; e-mail: santilli@iq.unesp.br.

<sup>†</sup> Instituto de Química/UNESP.

<sup>‡</sup> Synchrotron SOLEIL.

hydrosol prepared with different molar ratios,  $R_S$ , was monitored in situ by quasi-elastic light scattering (QELS) and rheological property measurements. These results were analyzed by using the mass fractal growth model.<sup>16</sup> The structural modification occurred in the bulk and on the surface of inorganic building blocks after reversible and irreversible aggregate growth was elucidated by extended X-ray absorption fine structure (EXAFS) and Raman spectroscopy measurements.

## 2. Experimental Procedures

**2.1. Synthesis.** Thermoresponsive hydrosols were prepared by the procedure previously described,<sup>12,13</sup> essentially consisting of  $\text{ZrOCl}_2 \cdot 8\text{H}_2\text{O}$  (Aldrich) dissolution in hydrochloric aqueous solution ( $2 \text{ mol L}^{-1}$ ) followed by addition to a hot ( $80^\circ\text{C}$ ) sulfuric acid aqueous solution ( $0.2 \text{ mol L}^{-1}$ ), drop by drop, under magnetic stirring. The volume of the  $\text{ZrOCl}_2$  solution was adjusted to yield suspensions with  $R_S = 2.5, 3.0, 4.0$ , and  $15.0$ . Aliquots of  $15 \text{ mL}$  of suspensions were put inside acetylcellulose membrane tubing ( $12\text{--}14 \text{ MW}$ ) and submitted to static dialysis against  $200 \text{ mL}$  of distilled water at room temperature (RT) for  $24 \text{ h}$  to obtain transparent suspensions.

**2.2. Rheology and Light Scattering.** The time and temperature evolution of viscoelastic properties during the gelation process was followed by dynamic oscillatory measurements carried out with a controlled-stress rheometer (Carri-Med-CLS100), equipped with plate–plate tools  $60 \text{ mm}$  in diameter and a  $400 \mu\text{m}$  gap between plates. The first set of measurements, concerning the determination of the gel temperature,  $T_{\text{gel}}$ , was carried out at a constant heating rate ( $0.5^\circ\text{C}$ ), and the applied stress was fixed at  $1 \text{ Pa}$ . The temperature sweep was repeated with different values of constant frequency at each run. The second set of experiments, concerning the time evolution of the viscoelastic properties, was carried out under isothermal temperatures lower than  $T_{\text{gel}}$ . The frequency, torque, and displacement were kept constant at  $0.05 \text{ Hz}$ ,  $0.1 \text{ Nm}$ , and  $1 \text{ mrad}$ , respectively. In situ QELS measurements were performed during gelation at the same temperature as those used for rheological monitoring, using a solid-state laser ( $25 \text{ mW}$ ,  $\lambda = 532 \text{ nm}$ ), a goniometer (Brookhaven BI200SM), and a photocalorator (PCS100). The error in the effective particle diameter measured during the experiment was  $\sim 5\%$ , given by the equipment.

**2.3. Raman Spectroscopy and EXAFS.** The Raman spectra of the thermoreversible sol was measured in situ during a cyclic variation of temperature using a commercial Raman spectrometer (model HL5R of Kaiser Optical Systems, Inc.) equipped with a near-IR laser diode working at  $785 \text{ nm}$ , operating with a laser power output of  $200 \text{ mW}$ . The beam was focused using a long working distance objective lens into a quartz cell, which was mounted in a thermostated block. The spectra of sol and gel samples were recorded with an integration time of  $1500 \text{ s}$ , between  $100$  and  $3000 \text{ cm}^{-1}$ . The dependence with temperature of the Raman band parameters of sulfate anions (peak position, peak intensity, and fwhm) was examined after cubic baseline correction. To evaluate components of complex band envelopes and to identify underlying spectral components, the iterative least-squares curve-fitting available on the GRAMS program was used assuming Gaussian band shapes. Wavenumber, bandwidths, and intensities were independent and unconstrained variables. Normalization of the integrated area of the bands corresponding to the symmetrical  $\nu_1$  mode was performed for the sol and gel samples to keep constant the total number of sulfate oscillators.

EXAFS data at the Zr K-edge ( $17998 \text{ eV}$ ) were collected on the EXAFS IV spectrometer (LURE-DCI) during a cycle in a

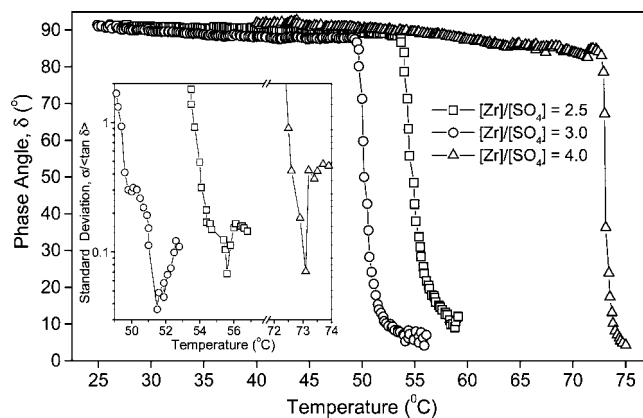


**Figure 1.** Temperature evolution of phase angle measured at an angular frequency of  $0.6 \text{ Hz}$  for sol prepared with  $R_S = 2.5, 3$ , and  $4$ . Inset shows gel temperature,  $T_{\text{gel}}$ , determined from the statistical loss factor ( $\sigma/\langle \tan \delta \rangle$ ) vs temperature.

temperature corresponding to the loss of reversibility behavior. These data were recorded simultaneously with Raman data using the original setup already described.<sup>17</sup> The monochromator was a Si(311) double crystal, and the experiment was performed in transmission mode using two ionization chambers filled with argon. EXAFS spectra were recorded within a  $1000 \text{ eV}$  energy range with  $2 \text{ eV}$  steps and a  $3 \text{ s}$  accumulation time per energy step. Data analysis based on the Fourier transform (FT) of the EXAFS spectra and on the least-squares fitting of the filtered EXAFS signals was carried out according to a procedure already described.<sup>12,13</sup>

## 3. Results

The effect of the  $[\text{Zr}]/[\text{SO}_4]$  molar ratio on the evolution of the phase angle ( $\delta$ ) measured at a fixed angular frequency ( $\omega$ ) of  $0.6 \text{ Hz}$ , during heating at a constant rate of  $0.5^\circ\text{C min}^{-1}$ , is presented in Figure 1. At low temperatures, the phase angle is constant and has a typical value of Newtonian fluid ( $\approx 90^\circ$ ). Above a given temperature, the phase angle abruptly decreases to values near  $0^\circ$ . This decrease of phase angle is characteristic of the transformation from a Newtonian fluid to an elastic solid due to the thermo-induced sol–gel transition. The gel temperature,  $T_{\text{gel}}$ , can be determined from this experimental data by using the constitutive equation proposed by Winter and Chambon<sup>18</sup>

$$\tan \delta(\omega) = \tan\left(\frac{\Delta\pi}{2}\right) = \text{constant at gel point; } 0 < \Delta < 1 \quad (1)$$

According to this definition, the function  $\tan \delta = f(T)$  measured at several frequencies presents a single intersection point at the critical transformation temperature ( $T_{\text{gel}}$ ). However, experimental curves display a dispersion of this crossover point due to random error, and therefore, the use of standard deviation  $\sigma$  of the mean  $\langle \tan \delta \rangle$  measured at different oscillatory frequencies is a convenient statistical tool to find  $T_{\text{gel}}$ . Accordingly,  $T_{\text{gel}}$  corresponds to a minimum of the curve  $\log(\sigma/\langle \tan \delta \rangle)$  as a function of temperature, shown in the inset of Figure 1. These results evidence that sol–gel transformation for the sample prepared with  $R_S = 3$  occurs at lower temperatures ( $T_{\text{gel}} = 50.5 \pm 0.2^\circ\text{C}$ ) than for the sol with  $R_S = 2.5$  ( $T_{\text{gel}} = 55.6 \pm 0.2^\circ\text{C}$ ) and  $R_S = 4$  ( $T_{\text{gel}} = 73.1 \pm 0.2^\circ\text{C}$ ). Furthermore, the experimental value of the gel relaxation exponents ( $\Delta = 0.71 \pm 0.3$ ) is equal to that predicted by scalar percolation theory.<sup>19</sup>

As the sol evolves quickly through the sol–gel transition and its properties change drastically, it is impossible to perform

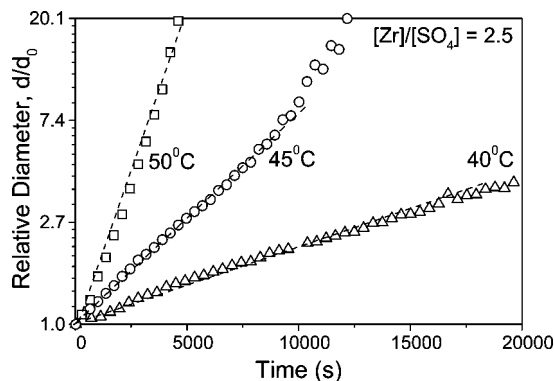


**Figure 2.** Time evolution of relative effective diameter ( $d/d_0$ ) of a sol prepared with  $R_S = 2.5$ . Continuous lines are the least-squares fitting of eq 3 with correlation coefficients of 0.986, 0.988, and 0.993 for data corresponding to samples at 40, 45, and 50 °C, respectively.

precise monitoring of the kinetic process when the system is maintained at isothermal temperatures close to  $T_{gel}$ . Thus, the investigation of isothermal evolution of each sol prepared with different  $R_S$  ratios was carried out at a temperature range lower than  $T_{gel}$  ( $T_{gel} - 25 < T < T_{gel} - 5$ ). To examine the evolution of the sol structure, as a function of time during the thermo-induced gelation processes, we utilized the fractal growth model proposed by Pope and Mackenzie,<sup>16</sup> such that

$$\ln(\eta_{sp}) = \ln\left(\frac{QL}{\rho_0}\right) + (3 - D)qt \quad (2)$$

This relationship describes the increase of the specific viscosity ( $\eta_{sp}$ ) of a suspension of spheroidal primary particles during the growth of fractal objects with dimensionality  $D$ ,  $Q$  being the mass concentration of the monomer,  $L$  a geometrical shape constant,  $\rho_0$  the density of primary particles, and  $q$  the growth constant rate. As we have previously shown, the growth constant rate  $q$  of different gelling systems follows an exponential relationship,<sup>20</sup> such that

$$\frac{d(t)}{d_0} = \exp(qt) \quad (3)$$

where  $d(t)/d_0$  is the size of a growing particle ( $d(t)$ ) normalized by its initial size ( $d_0$ ).

The time evolution of the relative effective hydrodynamic diameter ( $d(t)/d_0$ ) measured by QELS for the sol prepared with  $R_S = 2.5$ , plotted in a semilogarithmic scale, is shown in Figure 2. The linear dependence predicted by eq 3 is apparent for all presented data. The growth rates,  $q$ , obtained from least-squares fitting (with a correlation coefficient higher than 0.986) are  $0.7 \times 10^{-4}$ ,  $2.2 \times 10^{-4}$ , and  $6.3 \times 10^{-4} \text{ s}^{-1}$  for samples at 40, 45, and 50 °C, respectively. An analogous behavior was found for sols prepared with  $R_S = 3$  and 4. However, the apparent activation energy,  $E_a$ , of the growth process calculated from the Arrhenius plot ( $\ln q$  vs  $1/T$ ) exhibited a dependency on the  $R_S$  value (i.e.,  $E_a = 185$ , 227, and 142 kJ mol<sup>-1</sup> for  $R_S = 2.5$ , 3.0, and 4.0, respectively). It is important to note that the  $E_a$  sequence is equal to that observed for  $T_{gel}$  (Figure 1).

The logarithm of the specific viscosity as a function of transformation time at lower and higher temperatures corresponding to each  $R_S$  ratio is shown in Figure 3, panels a and b respectively. The trend followed by the curves can be fitted by two straight lines at the early and intermediary time periods. These results suggest that two different growth regimes occur in these stages of thermally induced transformation. The fractal dimensionalities determined from the slopes of these straight

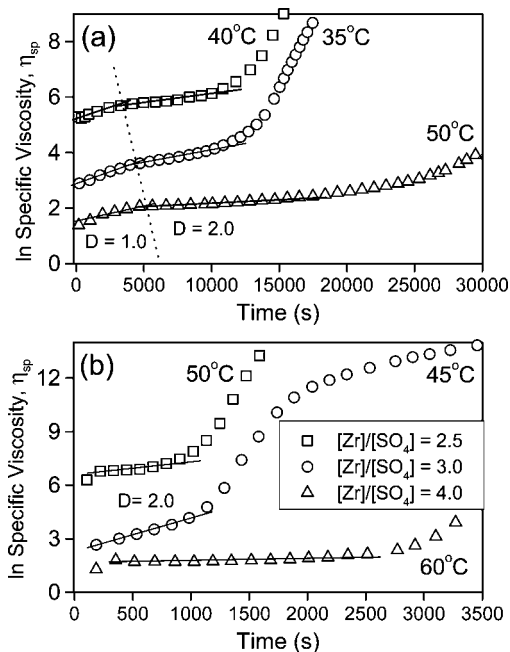


**Figure 3.** Natural logarithm of specific viscosity ( $\eta_{sp}$ ) vs time for the suspension with  $R_S = 2.5$ , 3.0, and 4.0. Continuous lines show the least-squares fitting of eq 2 with correlation coefficients of 0.994, 0.997, and 0.987, respectively. (a) Low and (b) high isothermal temperatures.

lines (eq 2) and from the growth rate constant are  $1.0 \pm 0.1$  and  $2.0 \pm 0.1$  for the early and intermediary stages, respectively. This finding indicates the formation of linear objects at the early stage ( $D = 1$ ), whereas the dimensionality of  $D = 2$  observed at the intermediate stage can represent both growth fractal and nonfractal (bidimensional particles of uniform density) structures. It is noteworthy that the early step is not observed at the higher temperature (Figure 3b) and becomes ill-defined as the  $R_S$  value decreases (Figure 3a).

The role played by the sulfate groups on the reversibility of the thermo-induced sol–gel transformation was analyzed by Raman spectroscopy. The spectra in the 940–1300 cm<sup>-1</sup> frequency range recorded during a thermoreversible cycle (cycle 1: sol (25 °C) to gel (2 h at 70 °C) to sol (15 h at 25 °C)) and under an irreversible cycle (cycle 2: sol (25 °C) to gel (7 h at 85 °C) to gel (60 h at 25 °C)) are presented in Figure 4, panels a and b respectively. This frequency range corresponds to the  $\nu_1$  (940–1100 cm<sup>-1</sup>) and  $\nu_3$  (1100–1300 cm<sup>-1</sup>) modes of sulfate-hydrogenosulfate anions.<sup>21</sup> The data are compared to RT Raman spectra of a freeze-dried sol ( $R_S = 3.0$ ) and of a thermostable sol ( $R_S = 15$ ). The band parameters of the  $\nu_1$  mode obtained by a Gaussian fitting procedure are reported in Table 1, together with the band assignments.<sup>22</sup> As this mode partly overlaps the  $\nu_3$  mode, the fitting procedure reported in Table 1 also takes into account the fitting of the 1100–1300 cm<sup>-1</sup> region using two additional Gaussian functions centered at  $1134 \pm 1$  and  $1200 \pm 1 \text{ cm}^{-1}$  for the RT sols. The contributions for the symmetric stretching mode  $\nu_1$  are split in the RT sols into four bands, centered at  $985 \pm 1$ ,  $1006 \pm 1$ ,  $1049.5 \pm 1$ , and  $1078.5 \pm 1 \text{ cm}^{-1}$ . If the attribution of the bands at 985 and 1006 cm<sup>-1</sup> is quite immediate, the assignment of the one around 1049.5 cm<sup>-1</sup> is less straightforward. Nevertheless, we note that this band is twice as broad as that observed for the thermostable sol ( $R_S = 15$ ) for which the low sulfate content should give rise to the dominant presence of a coordinated sulfate species. This suggests that the broad band around 1049.5 cm<sup>-1</sup> is made of



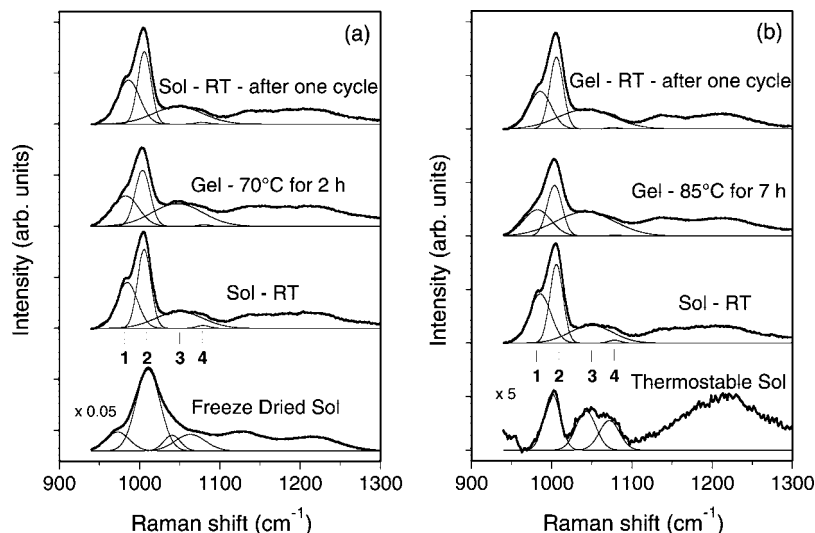


**Figure 4.** Raman spectra of sols with  $R_s = 3.0$  submitted to thermal cycles (a) preserving the reversibility of the sol–gel transition (cycle 1) and (b) leading to an irreversible gel (cycle 2). Raman spectra of a freeze-dried sol prepared with  $R_s = 3.0$  and of a thermostable sol with  $R_s = 15.0$  also are shown. The four component bands in the  $\nu_1$  sulfate region obtained by a Gaussian fitting procedure are displayed.

**TABLE 1: Maximum Position, fwhm, and Area of Bands Corresponding to Symmetrical Mode,  $\nu_1$ , of Sulfate Anions Present in Thermoreversible Sol and Gel ( $R_s = 3$ ), Thermostable Sol ( $R_s = 15$ ), and Freeze-Dried Thermoreversible Sol ( $R_s = 3$ )**

sample	peak 1			peak 2			peak 3			peak 4		
	position (cm <sup>-1</sup> )	fwhm (cm <sup>-1</sup> )	area	position (cm <sup>-1</sup> )	fwhm (cm <sup>-1</sup> )	area	position (cm <sup>-1</sup> )	fwhm (cm <sup>-1</sup> )	area	position (cm <sup>-1</sup> )	fwhm (cm <sup>-1</sup> )	area
Cycle 1												
sol at RT	984.6	30.0	14333	1005.7	19.6	16145	1049.5	68.2	11988	1078.5	17.4	552
gel at 70 °C	982.5	38.4	12108	1003.8	22.1	12910	1047.2	74.2	17462	1080.4	16.5	272
sol at RT	986.2	32.7	14984	1006.0	19.4	14619	1047.9	72.5	13158	1078.1	17.6	354
Cycle 2												
sol at RT	985.8	31.4	15291	1006.1	19.3	15079	1049.2	62.9	11041	1078.5	17.4	502
gel at 85 °C	982.3	40.1	10363	1003.7	21.9	10999	1041.8	86.2	20601	1079.6	14.7	168
gel at RT	985.8	32.5	12095	1006.1	19.8	14118	1042.6	81.4	15717	1076.7	16.0	254
sol $R_s = 15$				1000.8	23.7	2653	1042.9	29.2	2260	1072.0	29.3	1726
freeze-dried sol	972.6	34.7	134585	1010.6	35.1	594386	1040.5	24.4	80083	1063.1	44.0	151077
assignment	SO <sub>4</sub> <sup>2-</sup> free and adsorbed			SO <sub>4</sub> <sup>2-</sup> monodentate			SO <sub>4</sub> <sup>2-</sup> bidentate, HSO <sub>4</sub> <sup>-</sup> free			SO <sub>4</sub> <sup>2-</sup> tridentate		

two main contributions, one due to bidentate sulfate anions and one to free hydrogenosulfate HSO<sub>4</sub><sup>-</sup> ions.<sup>21</sup>

Upon heating, the positions of the three dominant  $\nu_1$  bands shift to lower frequencies by  $\sim 3$ – $10$  cm<sup>-1</sup>. Simultaneously to the peak shifts, the widths of the first (at 985 cm<sup>-1</sup> in the sol) and third (at 1049.5 cm<sup>-1</sup> in the sol)  $\nu_1$  bands continuously increase with temperature. In contrast, the width of the second peak (at 1006 cm<sup>-1</sup> in the sol) is nearly temperature invariant. Upon heating, a decrease of the number of sulfate oscillators in the two first  $\nu_1$  bands is evidenced by a decrease of the normalized areas, whereas an increase of oscillators is observed in the third  $\nu_1$  band. Upon a thermoreversible sol–gel transition (cycle 1), the changes of the band characteristics are quite reversible in position, bandwidth, and area. It is noteworthy that the bandwidths reported for the  $\nu_3$  mode at  $1134 \pm 1$  and  $1200 \pm 1$  cm<sup>-1</sup> present also similar reversible broadenings with temperature. The bandwidths and positions of the peaks at 985 and 1006 cm<sup>-1</sup> for the sol (reversible) and gel (irreversible) samples, both recorded at RT after a thermal cycle, do not present strong differences with the initial sols. But, a decrease of the area of the band centered at 985 cm<sup>-1</sup> is evidenced after irreversible gelation (cycle 2), indicating a decrease of the number of uncoordinated sulfate anions after the complete thermal cycle. Concomitantly to this area decrease, a shift of

the position of the third  $\nu_1$  band from 1049.5 cm<sup>-1</sup> (sol at RT) to 1042.6 cm<sup>-1</sup> together with an increase of its band area also is observed.

To go further on the knowledge of the structure of the primary particles in sol and irreversible gel samples, EXAFS measurements were carried out simultaneously with the Raman data for cycle 2. The data corresponding to the thermoreversible sol–gel transition already were discussed in ref 12 and led us to identify the primary building blocks as an analogue of Zr<sub>18</sub>O<sub>4</sub>(OH)<sub>36</sub>(SO<sub>4</sub>)<sub>14</sub> molecular units. The main conclusion was that no change of the local order around Zr occurs during a thermal cycle where the thermoreversibility is verified. Figure 5 displays the FTs recorded during cycle 2, corresponding to the loss of thermoreversible behavior. FTs are characterized by two peaks: the first one is related to the oxygen coordination shell as nearest neighbors and the second one mainly to zirconium contributions at larger distances. The first oxygen coordination shell is made of two contributions: one of  $3.6 \pm 0.5$  oxygen atoms at  $2.14 \pm 0.02$  Å and the second of  $2.6 \pm 0.5$  oxygen atoms at  $2.27 \pm 0.02$  Å. The main modification observed during the thermal cycle is a variation of the intensity of the second peak, which is due to a change of the Debye–Waller factors as evidenced by the values determined by the least-squares fitting procedure reported in the inset of

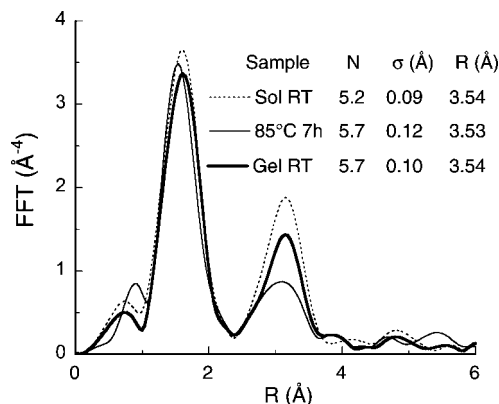


**Figure 5.** FTs of Zr K-edge EXAFS spectra recorded during cycle 2. The structural parameters ( $N$ ,  $\sigma$ , and  $R$ ) for zirconium second nearest neighbors obtained by a least-squares fitting procedure also are given. The agreement factors are 0.88, 0.51, and 0.42% for the sol at RT, gel at 85 °C, and gel at RT, respectively.

Figure 5. It is important to note that the first and second coordination shells of oxygen and zirconium atoms (coordination number and distance) are nearly invariant upon a thermal cycle leading to irreversible gelation. This gives evidence that neither in thermoreversible gelation nor in irreversible gelation are new oxo bridges between zirconium atoms formed.

#### 4. Discussion

The observed dependence on activation energies for aggregate growth and gel temperature with  $R_S$  is a general feature of a kinetically controlled process.<sup>5</sup> In that case, the transformation proceeds by a sequential process involving structural and compositional modifications of precursors and intermediate species with increasing stability, rather than a single step pathway.<sup>5</sup> The corresponding structural changes are usually closely associated with the effects of additives on the surface and/or interior of the preformed building block. A clear manifestation of this multistep process is early monodimensional growth followed by bidimensional or fractal ( $D = 2$ ) growth evidenced during the isothermal sol–gel transformation (Figure 3). Also, comparison between the curves presented in Figure 3 provides evidence that the linear growth regime becomes well-defined when the isothermal temperature is far from  $T_{\text{gel}}$  and when  $R_S$  increases from 2.5 to 4. In other words, a change in the growth process from bidimensional (or fractal with  $D = 2$ ) to linear growth decreasing the isothermal temperature (or the aggregation rate) and/or increasing the  $R_S$  ratio is expected.

We already demonstrated that one-dimensional growth of zirconia-based fibers can be obtained by the slow aggregation process of the thermostable sol ( $R_S = 15$ ) soaked with hexagonal SLC.<sup>15</sup> These fibers present a hierarchic structure made by the aggregation of microfibrils. As the dimensions of fibers are quite longer than the structural parameters of the SLC, the observed one-dimensional growth cannot result from a true templating mechanism.

To demonstrate bidimensional growth at a fast aggregation rate, we used a confinement strategy to avoid the secondary aggregation of particles. Indeed, direct drying of gels gives rise to compact face-to-face stacking of platelets, making difficult the easy observation of bidimensional particle morphology. Our confinement strategy consists of soaking the highly concentrated zirconium thermostable sol ( $R_S = 15$ ) with an oil (decahydronaphthalen)—surfactant (Igepal 850, Rhodia) mixture to produce a water–oil emulsion. The RT fast gelation was induced

by adding to this emulsion sulfuric acid until  $R_S = 3$  was reached. After extraction of volatile liquids by drying, a foam with 93% porosity was obtained (Figure 6). A closer observation shows that the foam pore walls are made of platelet-like particles. The pore wall morphology is quite different from the curved pore wall interface usually observed for liquid–liquid foam templating processes.<sup>6</sup> This clearly provides evidence that the dimensionality of the growth process is under kinetic control and that the  $[\text{Zr}]/[\text{SO}_4]$  molar ratio and temperature are two key parameters to regulate the anisometric growth of 1-D and 2-D particles.

The kinetic control of mono- and bidimensional growth can be explained by the molecular structure and surface properties of the primary building blocks. We already emphasized that the sols obtained in the thermostable domain and in the thermoreversible region (see the phase diagram reported in Figure 1 of ref 13) are made of the same primary building blocks described as an analogue of the  $\text{Zr}_{18}\text{O}_4(\text{OH})_{36}(\text{SO}_4)_{14}$  molecular units, for which the crystallographic structure was determined.<sup>14</sup> The main differences between the primary building blocks in the sols belonging to different regions of the phase diagram are the distribution of the sulfate anions at the surface of the blocks and the proportion of free sulfate anions in solution, as evidenced by Raman data (Figure 4). This distribution supports the use of the known crystallographic structure of the  $\text{Zr}_{18}\text{O}_4(\text{OH})_{36}(\text{SO}_4)_{14}$  molecular unit to propose a unified model for the growth of 1-D and 2-D particles. This model is displayed in Figure 7.

In agreement with the crystallographic structure reported for  $\text{Zr}_{18}\text{O}_4(\text{OH})_{36}(\text{SO}_4)_{14}$  (ref 14) and with the Raman results reported herein, three different sulfate complexing groups are present in the proposed primary building blocks (Figure 7a): two tridentate, 11 bidentate, and one monodentate sulfate anion. In the crystallographic structure,<sup>14</sup> two diagonally opposite monodentate sulfate anions link two adjacent building blocks, giving rise to linear arrangement of the units (Figure 7b). Our rheological data show that this linear growth is the first step of gel network formation. The reported EXAFS results strongly show that the oxo-hydroxo zirconium inner core of the primary building blocks is unaffected during irreversible gel network formation. In contrast, Raman data (Figure 4) show that the number of free and monodentate sulfate anions decreases during gel network formation, whereas the number of bidentate sulfate anions increases. This is evidence that the initial free and monodentate sulfate anions act as a network forming bridging primary building blocks in a linear framework (Figure 7b).

The first linear growth is followed by bidimensional growth as revealed by rheological data. It is quite evident that bidimensional growth results from the aggregation of linear chains. As a matter of fact, a closer examination of the linear framework displayed in Figure 7b shows that the bidentate and tridentate sulfate anions around the perimeter of the building block are located on two opposite surfaces parallel to the main axis of the chain. Because of the well-known ability of sulfate anions to participate in network propagation through hydrogen bonding, we propose that this peculiar distribution of sulfate anions leads to planar assembling by hydrogen bonding of the linear chains, as shown in Figure 7c. These hydrogen bonds should mainly involve free water molecules of the media.

Although the idealized model presented previously explains satisfactorily 1-D and 2-D growth of particles, the high sensitivity of the system to temperature and ionic strength as evidenced in ref 13 indicates that these sulfate solutions never reach an equilibrium state, as noted by Clearfield et al.<sup>14</sup> For

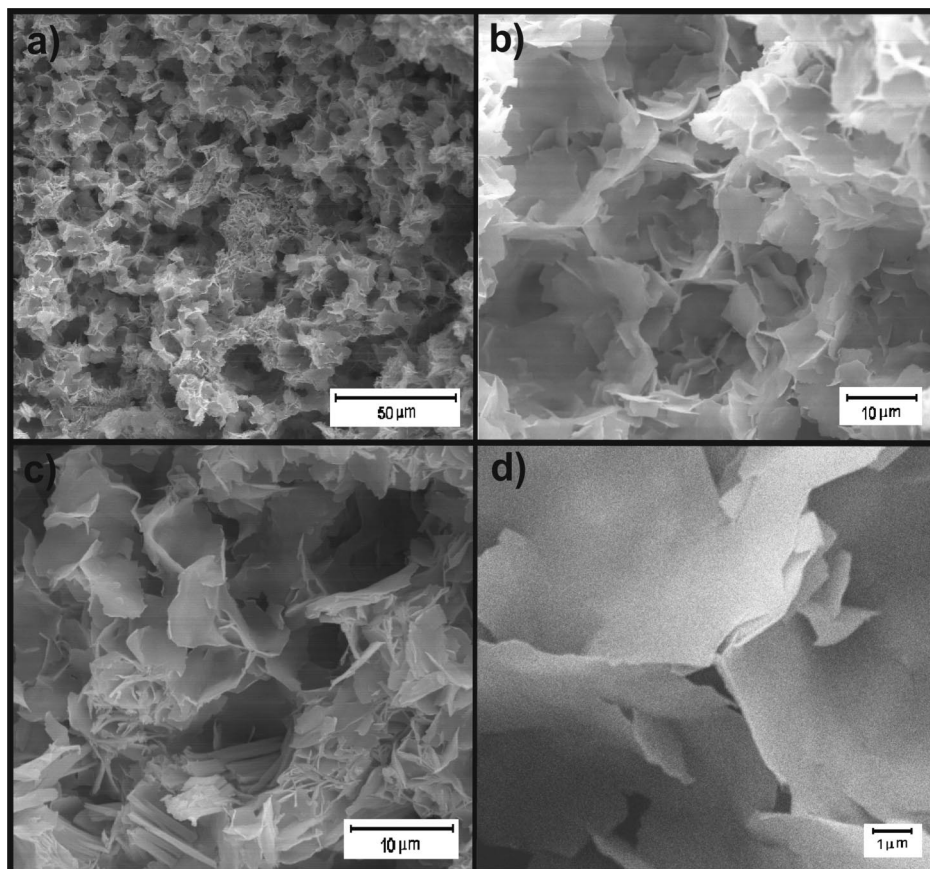


**Figure 6.** SEM micrographs of foam obtained after soaking the zirconium thermostable sol ( $R_s = 15$ ) in an oil (decahydronaphtalen)–surfactant (Igepal 850, Rhodia) mixture to produce a water–oil emulsion and adding sulfuric acid until  $R_s = 3$  was reached for inducing gelation. The magnification increases from panel a to panel d.

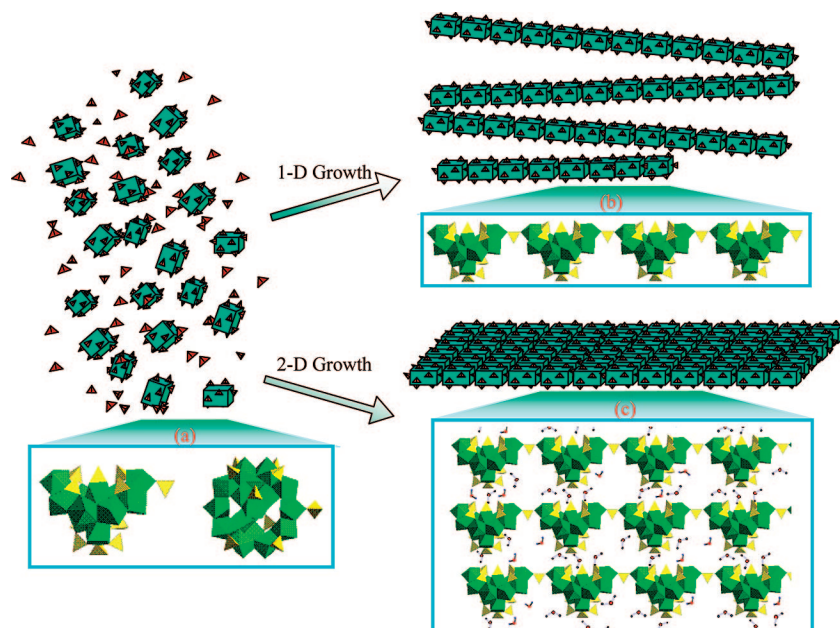


**Figure 7.** Schematic illustration of linear and planar growth process. (a) Two main projections of the zirconium basic sulfate building block ( $\text{Zr}_{18}\text{O}_4(\text{OH})_{36}(\text{SO}_4)_{14}$ ), (b) linear chain formed by bidentate sulfate bridges, and (c) growth of bidimensional structures by the formation of hydrogen bonds between surface complexed sulfate ions and surrounding water molecules.

instance, the huge increase in the bandwidth of free sulfate anions upon heating is a manifestation of the change of the first water solvation shell of free sulfate leading to a larger distribution of solvated species. This behavior is expected from the hydration enthalpy ( $-909 \text{ kJ mol}^{-1}$ )<sup>23</sup> of sulfate, which indicates that the degree of hydration should decrease sharply

by increasing the temperature. This favors the formation of ion pairing with a protonated surface of building blocks.<sup>24</sup> Indeed, the band centered at  $972.6 \text{ cm}^{-1}$  in the freeze-dried sol is due to adsorbed sulfate anions.<sup>21</sup> Then, we assume that the shift and enlargement of the mode related to the free sulfate anions observed upon sol heating (Table 1) also could result from this



adsorption process. The ion-pairing at the surface and the adsorption are a prerequisite for further coordination of sulfate with zirconium, as evidenced by the decrease in the number of free sulfates and increase of bidentate sulfate species. Our Raman results show that the equilibrium between complexation and solvation of sulfate anions can be easily reversed toward the release of coordinated sulfate, at early polymerization stages. On the other hand, this idealized model does not take into account possible ionic exchange between the sulfate network former and the chlorine structure breaker. This could lead to the formation of polynuclear species of lower molecularity, which could be involved in the overall network formation. Despite the complexity of the different equilibria involved in this system, our experimental results point out some rules to synthesize zirconia-based particles with different anisotropic shapes.

## 5. Conclusion

We studied the dynamics of a sol–gel transition under a controlled temperature (constant heating rate and isothermal conditions) for basic zirconium sulfate hydrosols prepared with different  $R_S = [\text{Zr}]/[\text{SO}_4]$  molar ratios. From the dependence of gelation temperature and apparent activation energy for the aggregate growth process with  $R_S$ , we conclude that the overall sol–gel transition is kinetically controlled by the relative amount of sulfate anions.

From in situ monitoring by QELS and dynamic rheological measurements under isothermal conditions, it was shown that the network formation involves two main stages: the formation of linear objects at the early stage ( $D = 1$ ) and the growth of bidimensional structures at the advanced stage ( $D = 2$ ). The overall results point out the control of the aggregation rate as the key parameter to regulate the production of powders with needle- and platelet-like particles. The growth from mono- to bidimensional particles can be shifted by increasing the aggregation rate. The original shape of the particles can be preserved after post-synthesis by using a confinement strategy.

Our detailed structural analysis by EXAFS and Raman spectroscopy allowed us to identify different sulfate species around the perimeter of the oxo-hydroxo zirconium building blocks. Among these species, one of them acts as a covalent network former, which is responsible for the linear linkage of the building blocks at early stages of the aggregation process. The other sulfate species can be considered as a covalent network breaker since the bidimensional growth is ensured through hydrogen bonding between the already formed linear

chains. The double antagonistic role of sulfate complexing ligands with respect to its network formation ability can be exploited in the control of particle shapes for other transition metal oxo-hydroxo building blocks.

**Acknowledgment.** This work was financially supported by FAPESP, CNPq, and CAPES/COFECUB. We acknowledge F. Villain (LCIM2, Paris 6) for help in using the Raman facility.

## References and Notes

- (1) Soten, I.; Ozin, G. A. *Curr. Opin. Colloid Interface Sci.* **1999**, *4*, 325–337.
- (2) Davis, M. E. *Nature (London, U.K.)* **2002**, *417*, 813–821.
- (3) Scott, B. J.; Wirnsberger, G.; Stucky, G. D. *Chem. Mater.* **2001**, *13*, 3140–3150.
- (4) Surendran, G.; Tokumoto, M. S.; Santos, E. P.; Remita, H.; Ramos, L.; Kooyman, P. J.; Santilli, C. V.; Bourgaux, C.; Dieudonne, P.; Prouzet, E. *Chem. Mater.* **2005**, *17*, 1505–1514.
- (5) Mann, S.; Colfen, H. *Angew. Chem., Int. Ed.* **2003**, *42*, 2350–2365.
- (6) Backov, R. *Soft Matter* **2006**, *2*, 452–464.
- (7) Mann, S. *Angew. Chem., Int. Ed.* **2000**, *39*, 3392–3406.
- (8) Elemans, J. A. A. W.; Rowan, A. E.; Nolte, R. J. M. *J. Mater. Chem.* **2003**, *13*, 2661–2670.
- (9) Peppas, N. A.; Hilt, J. Z.; Khademhosseini, A.; Langer, R. *Adv. Mater.* **2006**, *18*, 1345–1360.
- (10) Wang, H.; Holmberg, B. A.; Yan, Y. *J. Am. Chem. Soc.* **2003**, *125*, 9928–9929.
- (11) Chiavacci, L. A.; Santilli, C. V.; Pulcinelli, S. H.; Craievich, A. F. *J. Appl. Crystallogr.* **1997**, *30*, 750–754.
- (12) Chiavacci, L. A.; Pulcinelli, S. H.; Santilli, C. V.; Briois, V. *Chem. Mater.* **1998**, *10*, 986–993.
- (13) Chiavacci, L. A.; Santilli, C. V.; Pulcinelli, S. H.; Bourgaux, C.; Briois, V. *Chem. Mater.* **2004**, *16*, 3995–4004.
- (14) Squattrito, P. J.; Rudolf, P. R.; Clearfield, A. *Inorg. Chem.* **1987**, *26*, 4240–4244.
- (15) Santos, E. P.; Santilli, C. V.; Pulcinelli, S. H.; Prouzet, E. *Chem. Mater.* **2004**, *16*, 4187–4192.
- (16) Pope, E. J. A.; Mackenzie, J. D. *J. Non-Cryst. Solids* **1988**, *101*, 198–212.
- (17) Briois, V.; Belin, S.; Villain, F.; Bouamrane, F.; Lucas, H.; Lescouëzec, R.; Julve, M.; Verdager, M.; Tokumoto, M. S.; Santilli, C. V.; Pulcinelli, S. H.; Carrier, X.; Krafft, J. M.; Jubin, C.; Che, M. *Phys. Scr.*, **2005**, *T115*, 38–44.
- (18) Chambon, F.; Winter, H. H. *J. Rheol.* **1987**, *31*, 683–697.
- (19) de Gennes, P. G. *J. Phys. Lett.* **1976**, *37*, 1–2.
- (20) Sarmento, V. H. V.; Dahmouche, K.; Pulcinelli, S. H.; Santilli, C. V. *J. Mater. Chem.* **2005**, *15*, 3962–3972.
- (21) Niaura, G.; Malinauskas, A. *J. Chem. Soc., Faraday Trans.* **1998**, *94*, 2205–2211.
- (22) Rudolph, W. W.; Brooker, M. H.; Tremaine, P. R. *J. Solution Chem.* **1999**, *28*, 621–630.
- (23) Franks, G. V.; Johnson, S. B.; Scales, P. J.; Boger, D. V.; Healy, T. W. *Langmuir* **1999**, *15*, 4411–4420.
- (24) Rull, F.; Ohtaki, H. *Spectrochim. Acta, Part A* **1997**, *53*, 643–653.

JP803039P